Quispe *et al.*
Protection and Control of Modern Power Systems (2023) 8:22
https://doi.org/10.1186/s41601-023-00294-x

Protection and Control of
Modern Power Systems

ORIGINAL RESEARCH

Open Access

Time–frequency multiresolution of fault-generated transient signals in transmission lines using a morphological filter

Juan Carlos Quispe[1,2*], John Morales[1], Eduardo Orduna[1], Carlo Liebermann[3], Michael Bruhns[3] and Peter Schegner[3]

Abstract

The ongoing transformation of electrical power systems highlights the weaknesses of the protection schemes of traditional devices because they are designed and configured according to traditional characteristics of the system. Therefore, this work proposes a new methodology to study the fault-generated high frequency transient signals in transmission lines through multiresolution analysis. The high frequency components are determined by a new digital filtering technique based on mathematical morphology theory and a spectral energy index. Consequently, wide spectra of signals in the time–frequency domain are obtained. The performance of this method is verified on an electrical power system modeled in ATP-Draw, where simulation and test signals are developed for different locations, fault resistances, inception angles, high frequency noises, sampling frequencies, types of faults, and shapes of the structuring element. The results show the characteristics of the fault such as the traveling wave frequency, location, and starting time.

Keywords Digital filter, High frequency, Mathematical morphology, Time–frequency, Traveling waves

1 Introduction

The protection schemes and fault locating algorithms on Transmission Lines (TLs) are based on the use of the fundamental frequency. Therefore, these algorithms use phasors to calculate the impedance and the subsequent distance between the fault and protection relay.

One limitation of these methods is the dependence on the accurate extraction of the fundamental frequency phasors. In addition, the increase in the amount of power electronic equipment is causing challenges in electrical studies because they have the ability to control signals in both steady-state and fault conditions, which modifies the common behavior of the currents and voltages [1]. Also, it has been verified that the response time of inverter power control systems coincides with the operating time scale of the relays, resulting in more challenges to protection schemes [2]. Therefore, this means that the behavior of inverters is part of a new approach to studies in electrical systems as mentioned in [3]. Accordingly, the motivation arises to develop new methodologies that adapt to the operating characteristics of future power grids.

The use of transient signals as part of electrical fault studies again represents an attractive way of analysis, since it is based on instantaneous signals. Moreover, it only needs information from the first few milliseconds of the fault (< 10 ms), which makes it very attractive for fast fault clearance [4]. This study was born as a "noise" concept caused by short-circuits because Traveling Waves (TWs) affect the voltage and current waveforms when a fault occurs on a TL [5–7]. Thereafter, it has been studied

*Correspondence:
Juan Carlos Quispe
juancarlosqh@ieee.org
[1] Universidad Nacional de San Juan – CONICET, San Juan, Argentina
[2] Universidad Tecnológica del Perú, Lima, Perú
[3] Technical University of Dresden, Dresden, Germany

as a transient spectrum of a series of harmonics caused by TW where the presence of high frequency components in the signal is identified [8–11]. In that sense, new techniques that decouple the perturbation components from the base signal are the subjects of study, which implies an analysis in the time–frequency domain as shown in [12]. In addition, references [13] and [14] highlight that the behavior of the frequency spectrum of a fault provides information about its location, while [15] and [16] present protection studies based on this theory. This shows the great relevance of the study of transient components, although these methodologies require a suitable digital filter.

The extraction of fault information in different spectral frequency bands has been developed using the wavelet transform, which was introduced by Stephane Mallat [17]. The use of the wavelet transform was an alternative for processing high-frequency transient signals as shown in [18–24], in which their behavior for different frequency bands were studied. Many of these methods require only the TW arrival time information from the line terminals. This is used to extract the peaks caused by the TW in the voltage or current signals. Then, the difference in arrival times of the two-line terminals is used to determine the fault location. However, this method needs a communication channel and there is a risk of fault inception at the zero crossing of the voltage signal, in which circumstance the TW may not be clearly identified. On the other hand, methods based on multiresolution decomposition are performed over a limited range of frequencies, and high frequency components are not visualized thereby risking the loss of information. In addition, the wavelet transform breaks down a signal into frequency bands, which may not allow enough high resolution information to be obtained.

Techniques using mathematical morphology (MM) theory have become part of the study of transient signals, as explained in [25–28]. These studies develop a filter that suppresses the interference noise superimposed on the transient of TW, which is proven to be more efficient than the wavelet transform in filtering noises. However, they do not cover in depth the transient behavior of high frequency components for multiresolution analysis (MRA). The MM theory presents qualities to continue improving its methodological criteria and adapting to the applications required in power systems as mentioned in [29]. In this sense, the motivation arises to develop the MRA with high resolution and the lowest computational cost. Therefore, this work develops a method based on MM to determine the wide spectrum of high-frequency components as an application in digital processing for the Intelligent Electronic Device (IED) in TL, highlighting that the morphological method is suitable for analyzing signals with nonlinear characteristics and has the ability to extract frequency components with high resolution.

2 Fault-generated high-frequency transient signals

In electromagnetic transient (EMT) studies, the analysis of signals over different time scales is vital, although this involves dealing with a wide spectrum of frequencies. Therefore, it is convenient to characterize the components of the signal, which are mainly made up of components such as the information signal, base signal and noise, as shown in Fig. 1. These signals can be categorized according to their oscillating frequencies. The base signal is broad trending and the frequency range is low, normally at the rated 50 or 60 Hz of the electrical system. The noise signal, which it is desired to eliminate or mitigate as much as possible, generally occurs at a very high frequency. The information signal, which is of interest to process, is generally in the medium or high frequency range. Although there is no exact difference between the frequencies of the noise and the information signal, in this work the traveling wave effect is used as the information signal.

When a short-circuit occurs on a TL, TWs and resonances arise in voltage and current signals, affecting their waveforms. Furthermore, these signals contain a spectrum of high frequency and are associated with a series of harmonics, which in turn are related to the fault distance. In this sense, the study of fault-generated high frequency transient signals involves the analysis of TW features.

2.1 Reflection and refraction of traveling waves

The reflection and refraction phenomena of TW cause distortions in the electrical signals [5]. This distortion can be considered periodic, since the period depends on the impact instants of the TW and the reflection on the fault. This can be represented by a Lattice diagram as shown in Fig. 2.

As shown in Fig. 2a, when a TW generated by an electrical fault in the TL (Line L-R with line characteristic impedance Z_{1c}) impacts the terminals, it causes a reflected and refracted wave because of the change of propagation medium, i.e., the TW enters a new medium with different characteristic impedance of the adjacent line R-T or S-L. This effect is repeated as the wave finds new boundaries. However, this phenomenon is damped because the wave loses intensity at each

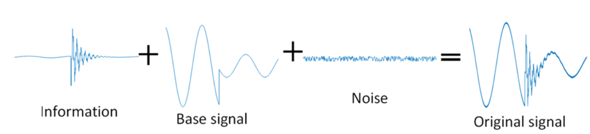

Fig. 1 Transient signal components

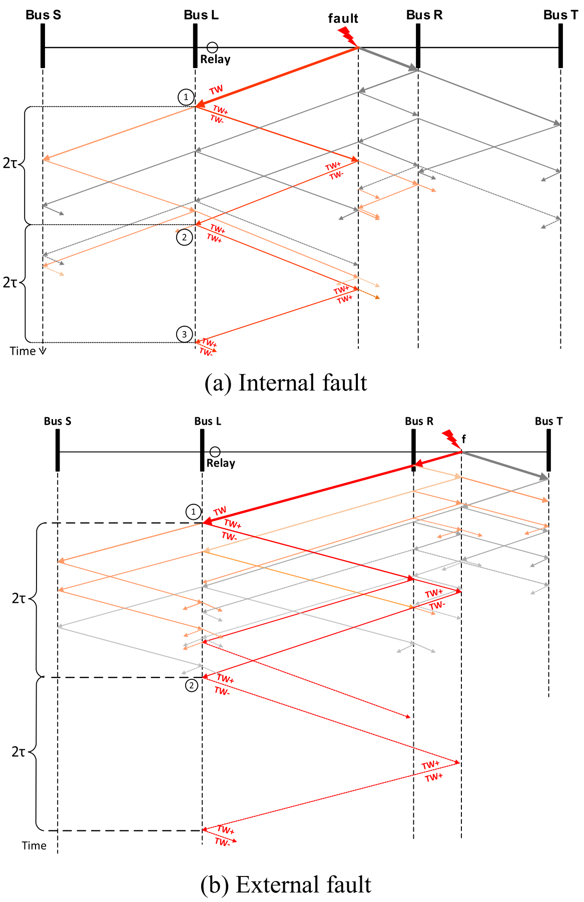

Fig. 2 Effect of reflection and refraction of TW by lattice diagram

impact. The magnitude and distribution of TW arrivals are affected by fault location, reflection coefficient and system topology. Therefore, a relay located on Bus L of the TL L-R detects the second fault-reflected impact after several previous arrivals. This impact caused by the reflection at the fault location takes 2τ time as shown in points 1 and 2 of the red arrows in Fig. 2a for an internal fault and Fig. 2b for an external fault (line R-T).

Figure 3 shows the magnitudes and arrival times of the TW signals caused by faults. The highest peaks or crests represent the impacts of the TWs due to reflection on the fault itself. This phenomenon leads to distortion of the base signal and is associated with a period, which implies the presence of the frequency of the traveling wave.

In order to calculate the period of the transient signal, the reflection coefficient (Γ_{TW}) plays an important role. In a test system shown in Fig. 4a, when the TW impacts Bus L, the reflected wave may be of positive or negative sign. This is determined by the relationship between the characteristic impedances of the two media as:

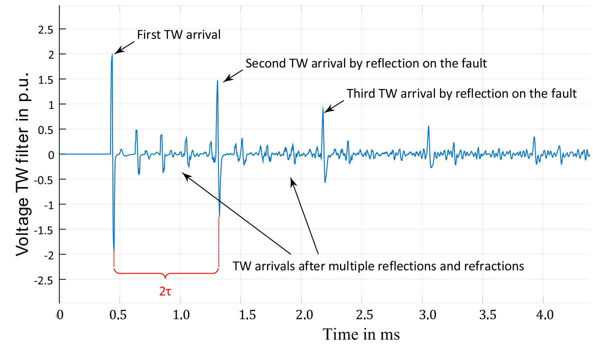

Fig. 3 Characteristics of the TW arrival time

$$\Gamma_{TW} = \frac{Z_{1C} - Z_0}{Z_{1C} + Z_0} \quad (1)$$

If Z_0 is greater than Z_{1c}, the TW backs to the fault with a negative sign, otherwise the TW backs to the fault with a positive sign. In the first case, the impact of the TW on the fault must be repeated twice to return to the initial case, and thus to repeat the cycle 4τ seconds must elapse. However, in the second case, the impact of the wave on the fault must be repeated once to return to the initial case, and the cycle is completed in 2τ seconds. This fact can be clearly identified in Fig. 4b.

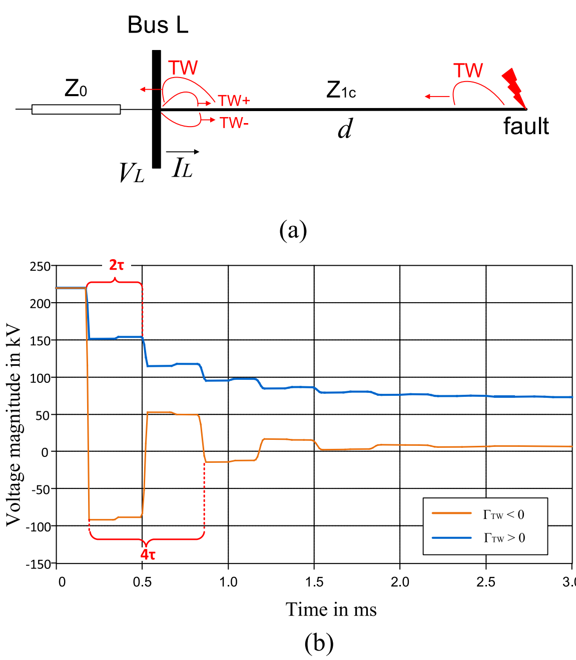

Fig. 4 Period of the transient signal for different reflection coefficient sign: **a** test system; **b** $\Gamma_{TW} < 0$, $\Gamma_{TW} > 0$

Consequently, there are two possible cases in the signal period (2τ and 4τ) where the traveling wave frequency is the inverse of their period:

$$Freq_{fault} = \frac{1}{4\tau}[Hz], \quad Z_0 = Large \tag{2}$$

$$Freq_{fault} = \frac{1}{2\tau}[Hz], \quad Z_0 = Small \tag{3}$$

where $\tau = d/v$ is the wave travel time from the fault location to Bus L, d is the fault distance in km, v is the TW speed in km/s (near the speed of light). The TW speed and the line characteristic impedance are determined by the inductance (L) and capacitance (C) of the TLs, with $v = 1/\sqrt{(LC)}$ in km/s, $Z_{1c} = \sqrt{(L/C)}$ in Ω. Considering the following representative values of L = 0.8467 mH/km and C = 0.014 uF/km for the 220 kV transmission line, then v = 290,450 km/s and Z_{1C} = 245.92 Ω. The frequency values associated with the fault distance are determined for both period cases as shown in Fig. 5.

3 Theoretical model

Georges Matheron and Jean Serra proposed the Mathematical Morphology theory, which is based on set theory [30]. This method was applied to signal processing of the one-dimensional non-linear type with good robustness [31]. It is based on four basic operations defined as dilation (⊕), erosion (⊖), opening (•) and closing (∘). The opening and closing are constructed operations based on the combination of dilation and erosion, as:

$$(f \oplus g)(x) = \max_m \{f(x+m) + g(m) | (x+m) \in D_f, m \in D_g\} \tag{4}$$

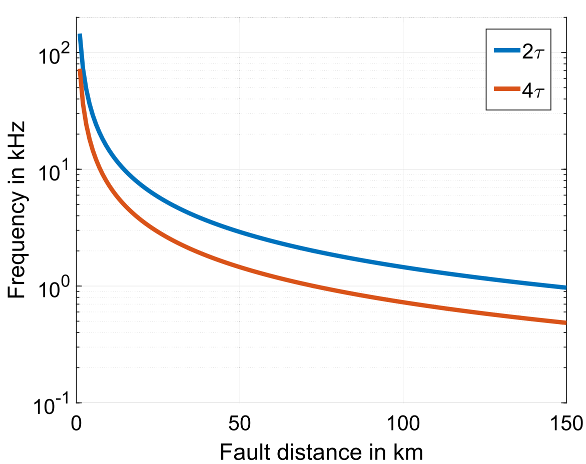

Fig. 5 Transient signal frequency behavior for different fault distances

$$(f \ominus g)(x) = \min_m \{f(x+m) + g(m) | (x+m) \in D_f, m \in D_g\} \tag{5}$$

$$(f \bullet g)(x) = [(f \oplus g) \ominus g](x) \tag{6}$$

$$(f \circ g)(x) = [(f \ominus g) \oplus g](x) \tag{7}$$

where $f(x)$ is the original one-dimensional discrete signal, $g(x)$ is the structuring element (SE) function, D_f and D_g are defined as the domains of f and g, respectively, and x is the signal sample. SE is a function used to interact with the main signal, and the aim is to obtain a match correlation between this function and the behavior of the signal.

3.1 Digital morphologic filter (DMF)

Two operators are defined to filter the noise in the signals, i.e., digital morphologic filter open-close and digital morphologic filter close-open using the same SE, shown as:

$$FM_{OC}f(x) = (f \circ g \bullet g)(x) \tag{8}$$

$$FM_{CO}f(x) = (f \bullet g \circ g)(x) \tag{9}$$

where FM_{OC} is the closing-opening morphological filter and FM_{CO} is the opening-closing morphological filter. Because of the reduction of the opening operation, the output of the opening-closing filter becomes smaller, and because of the expansion of the closing operation, the output of the closing-opening filter becomes larger [32, 33]. Therefore, a filter is built from the average value of the previous two filters shown in (8) and (9) as:

$$DMF_g f(x) = \frac{FM_{OC}f(x) + FM_{CO}f(x)}{2} \tag{10}$$

where DMF_g is the filter by mathematical morphology with "g" as the SE.

The SE can adopt different shapes and lengths which depend on the type of analysis to be performed. Some studies propose the use of a linear shape, but it is also possible to use triangular or sine shapes because transient signals have no defined form. In this sense, the sinusoidal, linear and triangle function are shown respectively in (11), (12) and (13) as:

$$g(n) = A \times \sin\left(\frac{\pi}{2}\left(1 + \frac{Le}{n}\right)\right), \quad Le = \left[-\frac{n}{2} : \frac{n}{2}\right] \tag{11}$$

$$g(n) = A, \quad Le = \left[-\frac{n}{2} : \frac{n}{2}\right] \tag{12}$$

$$g(n) = A\left(\frac{2 \times Le}{n} + 1\right), \quad Le = \left[-\frac{n}{2} : 0\right] \wedge$$
$$g(n) = A\left(\frac{-2 \times Le}{n} + 1\right), \quad Le = \left[0 : \frac{n}{2}\right] \tag{13}$$

where A is a constant that is the amplitude ($A > 0$), n is the level ($n > 0$) and Le is the SE length. Figure 6 shows the different shapes of the SE.

In that sense, the performance of digital filtering depends on the characteristics of the length and shape of the SE function.

3.2 Multiresolution analysis of signals based on DMF

The aim is to obtain signal information for different frequency ranges. The length of the SE indicates the level of resolution, and therefore the variation of the SE length gives the ability to obtain different frequency ranges, which are used for the construction of the multiresolution signal. The process is detailed as:

$$f_1(x) = FMM_{g1}f(x), \quad H_1(x) = f(x) - f_1(x) \tag{14}$$

where $f_1(x)$ is the filtered signal, g_1 is the SE and $H_1(x)$ represents the multiresolution signal at level "1". This analysis is repeated using an SE (g_2) with a new length:

$$f_2(x) = FMM_{g2}f_1(x), \quad H_2(x) = f_1(x) - f_2(x) \tag{15}$$

where $f_2(x)$ is the filtered signal from f_1, g_2 is the SE and $H_2(x)$ represents the multiresolution signal at level "2".

It is developed in a similar way for the following levels, and therefore, it can be generalized as:

$$f_n(x) = FMM_{gn}f_{n-1}(x), \quad H_n = f_{n-1}(x) - f_n(x) \tag{16}$$

$$f = f_n + \overbrace{f_{n-1} - f_n}^{H_n} + \cdots + \overbrace{f_1 - f_2}^{H_2} + \overbrace{f - f_1}^{H_1} \tag{17}$$

Finally, with this representation, it is possible to decompose the transient signals of the electrical faults in order to verify the signal characteristics in different frequency ranges.

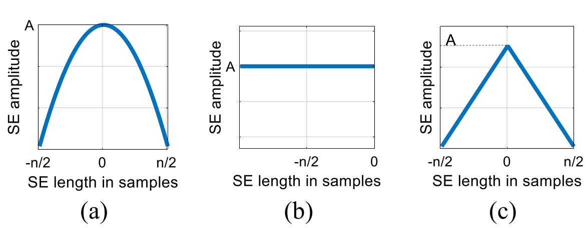

Fig. 6 Structuring element shapes: **a** sinusoidal shape, **b** linear shape and **c** triangular shape

3.3 Spectral energy index (SEI)

The spectral energy index or simply spectral energy is determined as the sum of the squares of the instantaneous voltage or current signal values as:

$$SEI_i = \sum_{k=1}^{N} (H_i)^2 k \Delta t \tag{18}$$

where SEI_i is the spectral energy for level i, H_i is the multiresolution signal (voltage or current) for level i, k is the summation index, N is the number of samples for a time window and Δt is the time interval of the signal which depends on the sampling frequency.

3.4 Multiresolution signal in time–frequency domain

The process starts with the detection of an electrical fault (short-circuit) on the TL. Then, the three-phase signals are read from the system, and the signals are extracted at a certain sampling frequency by means of analog/digital equipment (A/D conversion), which can be adapted to devices with different sampling frequencies. After that, the analysis time window is defined as 5 ms. The three-phase signals (abc) are transformed to modal signals (αβ0) by means of Clarke's transformation, where aerial (αβ) and ground (0) modal components are obtained. Thereafter, the signals are filtered using the DFM method and in this block the maximum level (M) of the MRA and the SE shape are set. In addition, for each level of calculation the result is stored in a multiresolution matrix (MR matrix). Figure 7 shows the flow chart of the methodology.

4 Case study analysis

4.1 Electric power system used

A 220 kV electric power system is developed in the software ATP-Draw for EMT simulations, as shown in Fig. 8a. The lengths of the TLs are 100 km (line L-R) and 80 km (line R-T). The model is based on the configuration of the tower structure shown in Fig. 8b, c, and the TLs are modeled using the JMarti method, which depends on the frequency. The IED as a measurement device is located on Bus L looking towards Bus R (L-R).

The MRA is developed for 120 multiresolution levels based on different SE lengths, and these values are measured in samples (6–1200 with 10-sample step). The selection of SE lengths is distributed as shown in Fig. 9. It is relevant to note that the highest resolution is presented for large values of SE length in order to have greater accuracy of the far faults, especially at the border of the lines (Bus R).

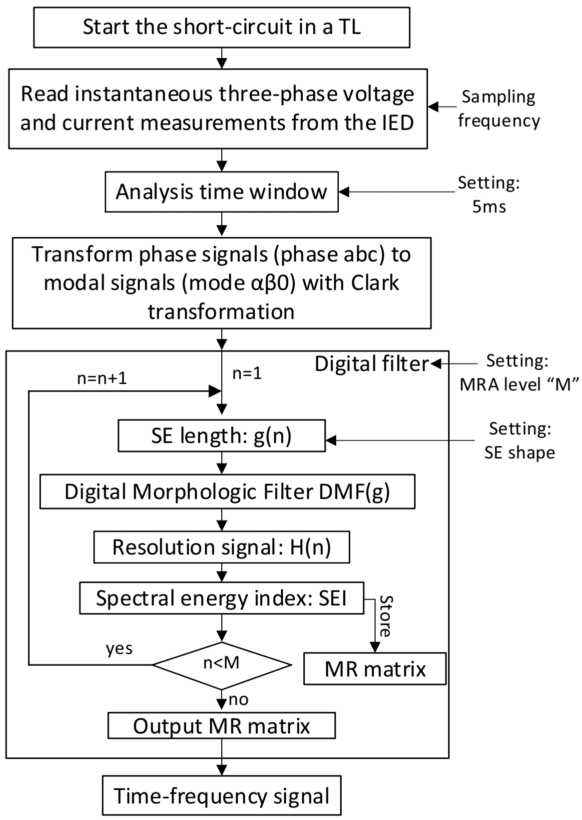

Fig. 7 Flow chart of the proposed method

In addition, different types of faults are simulated. They are affected by certain considerations:

- *Fault resistance* values of 0.01, 25 and 50 Ω.
- *Fault inception angle* it is verified for four instants, considering values close to the maximum and minimum points, and instants close to the zero crossing.
- *Fault location* five internal faults (1, 25, 50, 75 and 99 km) in the line L-R and three external faults (1, 15 and 30 km measured from R to T). In the external fault cases, the 100 km of the L-R line are added, resulting in distances of 101, 115 and 130 km.
- *Noise* in order to verify the robustness against noise, white Gaussian noise with signal-to-noise ratios (SNR) of 20, 30 and 40 dB with very high-frequency is added.
- *Sampling frequency* 1 MHz, 500 kHz and 100 kHz are considered.
- *SE shape* three different geometric shapes are considered.

4.2 Fault distance analysis

The frequency of the signal depends on the fault location as detailed in the theoretical section. Therefore, it is very important to know the predominant frequency in the multiresolution analysis. For this analysis, faults with distances of 1, 25, 50, 75, 99, 101, 115, 130 km are considered. Figure 10a shows four examples. Figure 10b shows the characteristics of the cases in the time–frequency domain, where the predominant frequency spectrum for each case can be clearly identified. Another highlight is the magnitude of the SEI intensity which decreases as the fault moves away as shown in Fig. 10c.

The values obtained are compared with the theoretical curve. Table 1 shows the relationship of the frequencies and the errors. As seen, in contrast to the first case, which has a high percentage of error because of low SE length approximation, the error percentages of the other cases are very low and good accuracy of the fault location is obtained as shown in Fig. 11. Using this method, multiresolution signals can be uniformly adjusted along the entire line for greater accuracy, and the spectrum can also be reduced. However, this incurs a higher computational cost, and so it can be used as an off-line fault locator. On the other hand, the resolution can be decreased in the first kilometers of the line and increased at the border of the lines, so this can be used as protection equipment in real time, one that identifies internal and external faults or a distance protection based on zones.

4.3 Influence of fault resistance

In order to verify the behavior of the method for different fault resistance values, 0.01, 25 and 50 Ω are considered. Figure 12 shows the maximum magnitudes of the SEI. These are 0.0153, 0.0138 and 0.0119 pu for each case respectively. Although it can be seen that the SEI decreases with the increase of resistance, the characteristics of the time–frequency signals remain intact since in all cases the frequency of the fault signal is identified at 1.428 kHz, which represents a fault distance of 50 km.

4.4 Influence of the inception angle

When analyzing the generation of TWs caused by short-circuits, care must be taken with the precise time at which the fault occurs, because faults that are very close to the zero crossing of the voltage signal do not generate prominent TWs. For this reason, many faults are verified for different inception angles, including very close to the zero crossing, the positive half-cycle and negative half-cycle as shown in Fig. 13.

In Fig. 14, the four cases are analyzed for a fault at 75 km. It can be seen that the third case presents lower transient components than the others and the maximum

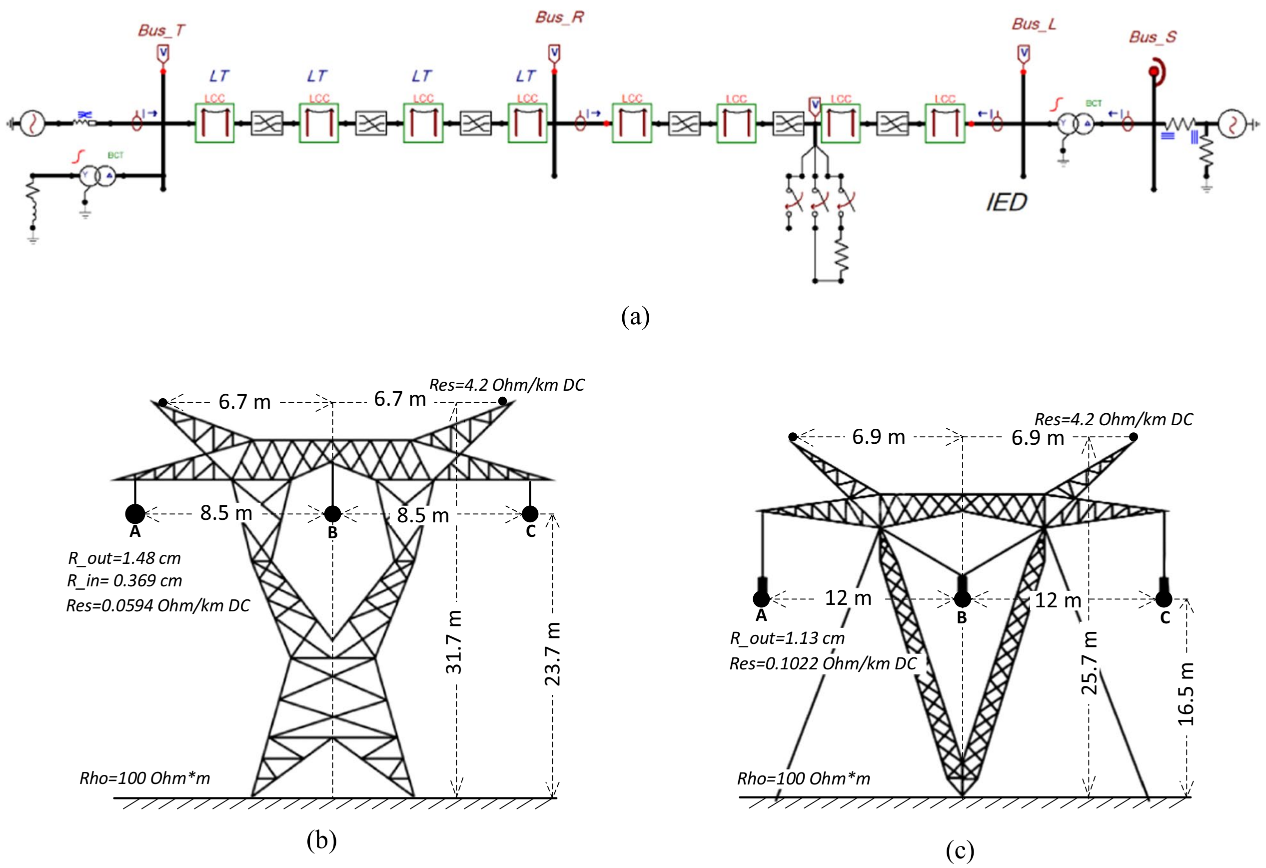

Fig. 8 Electric power system: **a** single line diagram; **b** tower configuration line L-R; **c** tower configuration line R-T

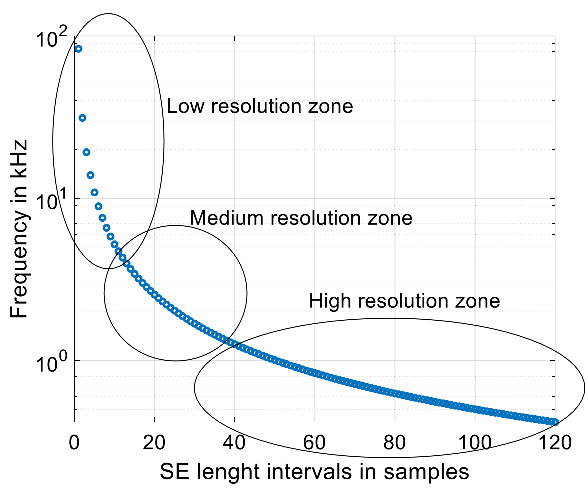

Fig. 9 Filtered frequency spectrum characteristics for each SE length interval

SEI reaches 0.0011 pu. However, in the time–frequency plots it is possible to identify, without distortions, the frequency of the signal for all cases. This frequency (0.961 kHz) corresponds to a fault at 75 km distant. In addition, the magnitude of SEI for the third case may be confused with distortions or noise only when faults are very far away.

4.5 Influence of high frequency noise

Noises emanate from different sources such as electrical network equipment, the measurement process, etc. This analysis considers the inclusion of white noise in the signals with SNR values of 20, 30 and 40 dB at very high frequencies. Figure 15 shows the spectral energy values for different frequency values (those on the left), and the maximum spectral energy index caused by the noise is verified by a horizontal dotted line. The maximum spectral energy for the signal without noise is 0.0016 pu, while the signals with noise have 0.0022, 0.0030 and 0.0055 pu for 40 dB, 30 dB and 20 dB, respectively. These values represent 8%, 8.8%, 12% and 22% with respect to the signal frequency for each case. Therefore, it is possible to clearly differentiate the analysis signal from the noise.

4.6 Influence of sampling frequency

As explained in the section on the theoretical model, the SE length is measured in samples, so it depends on

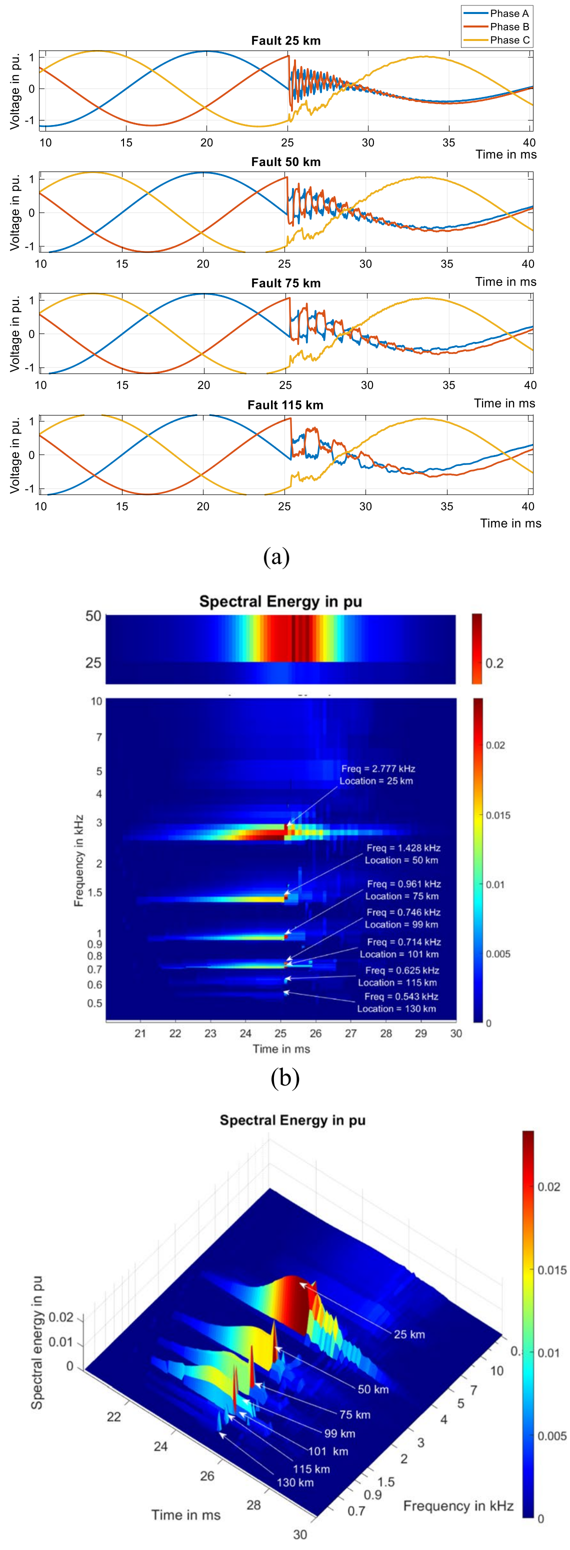

Fig. 10 Spectral energy for different fault distance characteristics: **a** two-phase fault; **b** 2D view of the MR matrix; **c** 3D view of the MR matrix

Table 1 Percentage error of frequency

Fault distance (km)	Frequency—theorical (kHz)	Frequency—simulation (kHz)	Error (%)
1	72.61	50.00	31.1
25	2.904	2.777	4.61
50	1.452	1.428	1.65
75	0.968	0.961	1.37
99	0.733	0.746	1.77
101	0.718	0.714	0.55
115	0.631	0.625	0.95
130	0.558	0.543	2.68

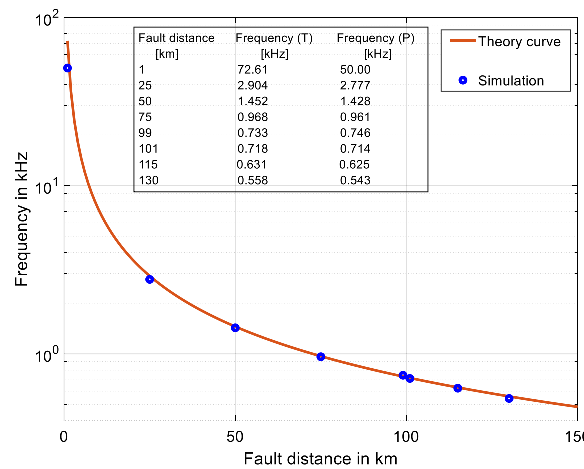

Fig. 11 Comparison of the frequencies obtained between the theoretical curve and the simulation points

the sampling frequency (Fs). A time window of 5 ms is considered for the analysis. The relationship between the sampling frequency and sample quantity is shown in Table 2 for three cases.

According to the Shannon Nyquist theorem [34], the sampling frequency must be greater than double the highest frequency component of interest in the measured signal. Thus, the maximum frequency component will be 500 kHz, 250 kHz and 50 kHz for the 3 sampling frequencies, respectively. However, almost all short-circuit events have frequencies lower than these values.

The traveling wave frequency of the signal components (multiresolution signals) is related to the values of the SE length as shown in Fig. 16, where there are three sampling frequencies. In order to analyze far away faults, frequencies up to approximately 0.250 kHz are considered for all three cases. The respective number of samples are 2000, 1000 and 200. These indicate the maximum signal resolution levels (N). In addition, the SE length can take smaller frequency ranges in a desired band, which means that it offers high frequency resolution for high frequency

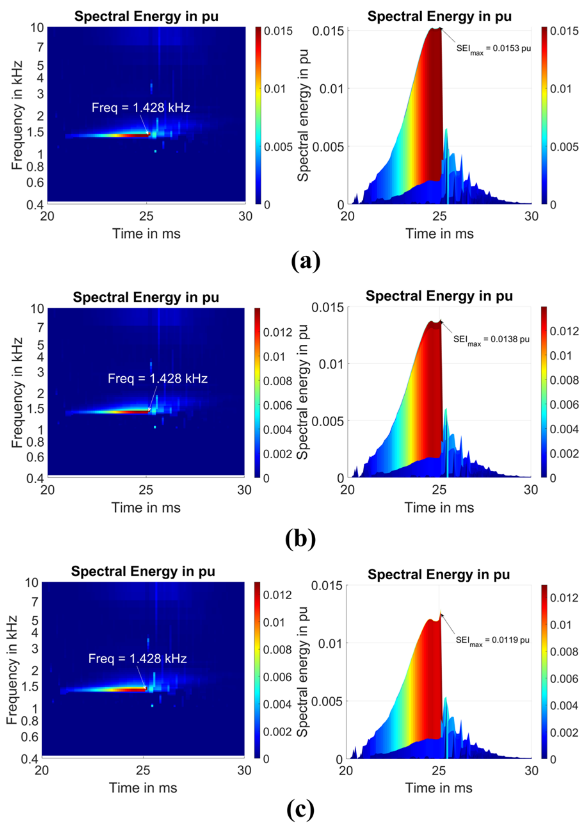

Fig. 12 Time–frequency for different fault resistances: **a** R = 0.01 Ω; **b** R = 25 Ω; **c** R = 50 Ω

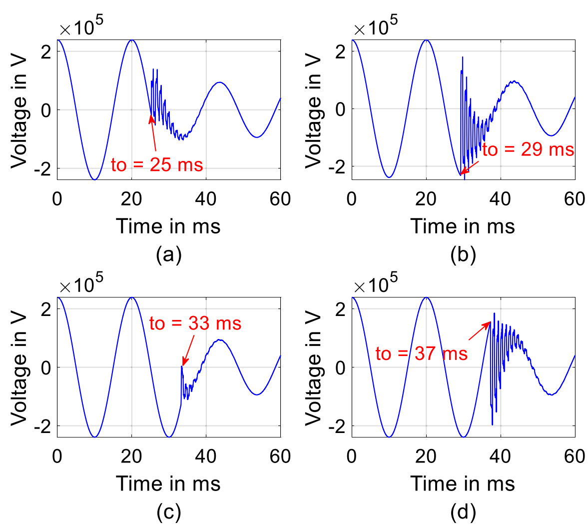

Fig. 13 Inception angle behavior: **a** to = 25 ms; **b** to = 29 ms; **c** to = 33 ms; **d** to = 37 ms

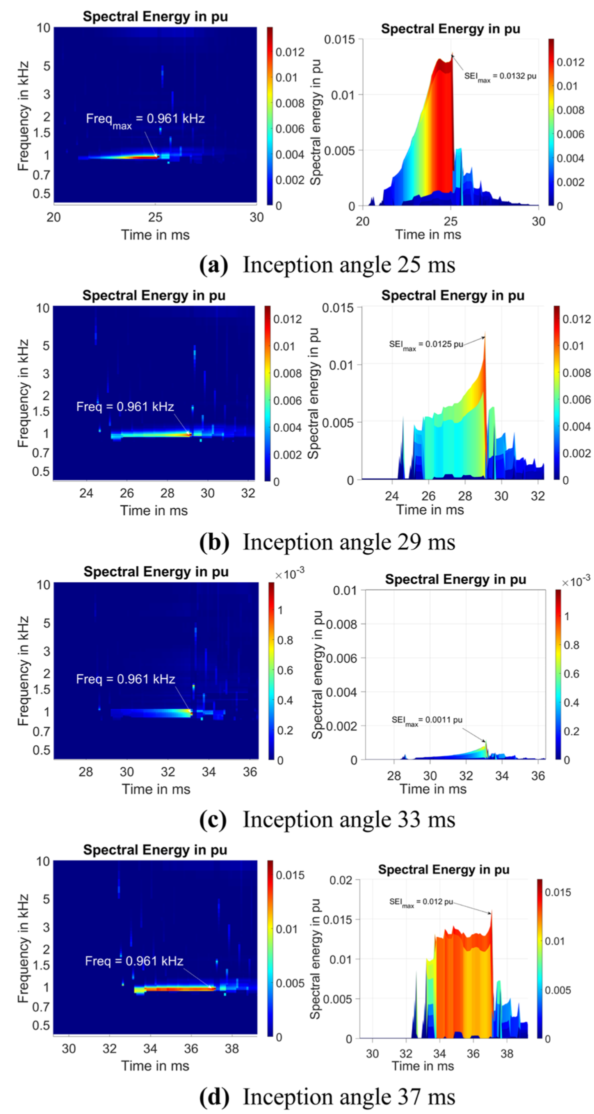

Fig. 14 Cases for influence of the inception angle

signals. This is different to the wavelet transform, which offers high time resolution but low frequency resolution for high frequencies, and high frequency resolution but low time resolution for low frequencies [35].

The analysis developed previously was carried out with a sampling frequency of 1 MHz. Only 120 multiresolution levels were considered, in order to avoid high computational effort. These levels were selected according to Fig. 9. For the study of signals with a sampling frequency of 500 kHz, SE length values from 5 to 600 with step of 5 samples are considered. Finally, for signals with a sampling frequency of 100 kHz, SE length values from 1 to 120 with a step of 1 sample are considered.

Figure 17 shows the results for a fault located at 50 km with different sampling frequencies while the

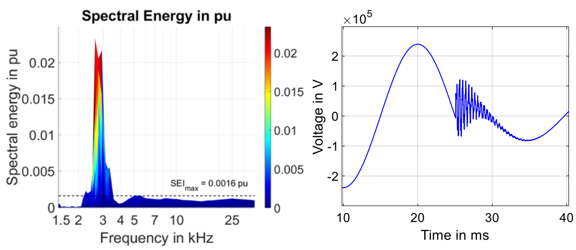

(a) Without SNR

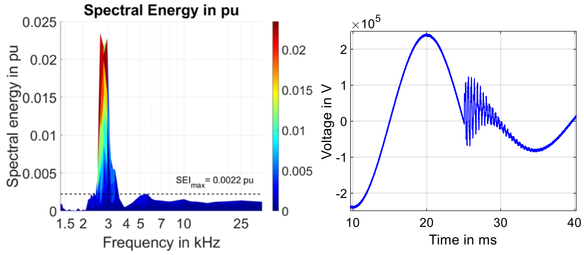

(b) SNR: 40 dB

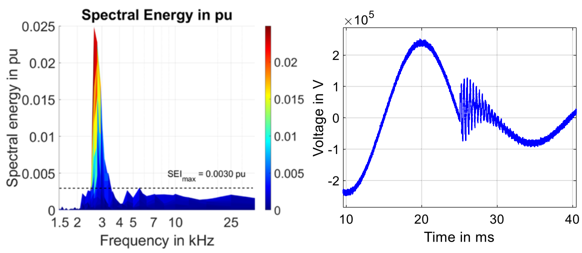

(c) SNR: 30 dB

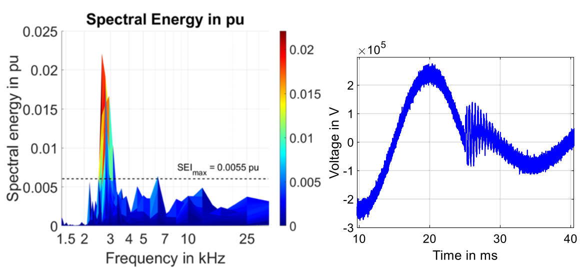

(d) SNR: 20 dB

Fig. 15 Very high-frequency noise

Table 2 Relationship between Fs and sample quantity

Sampling frequency (kHz)	Sample quantity
1000	5000
500	2500
100	500

expected signal frequency is 1.452 kHz. For the 1 MHz, the peak frequency value is 1.430 kHz and frequency range is [1.32–1.66] kHz, whereas for the 500 kHz, the peak frequency value is 1.453 kHz and frequency

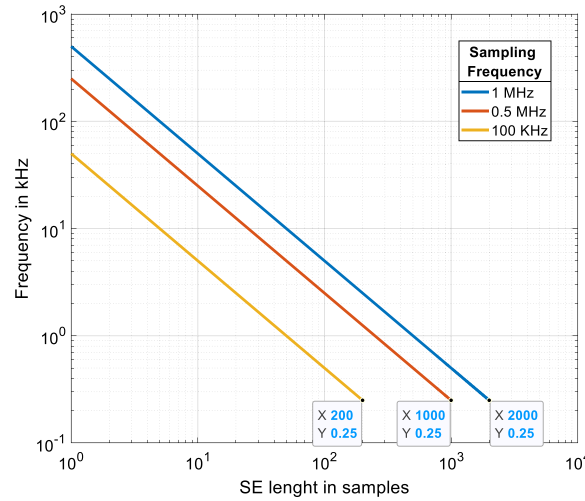

Fig. 16 Multiresolution signal frequencies versus SE length (logarithmic scale)

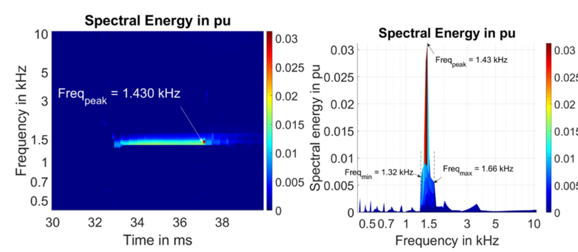

(a) Fs = 1 MHz

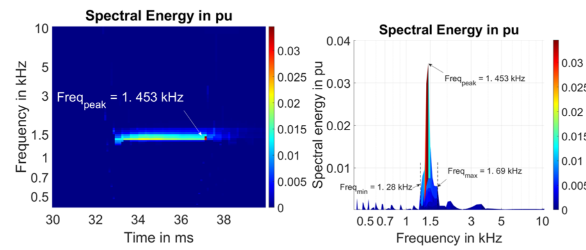

(b) Fs = 500 kHz

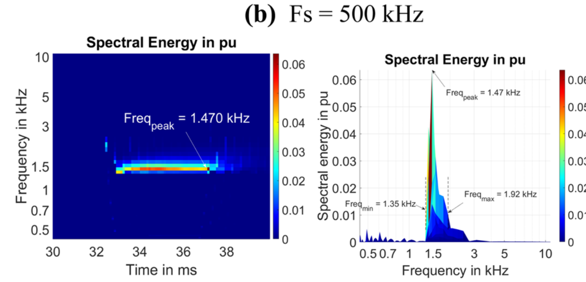

(c) Fs = 100 kHz

Fig. 17 Spectral energy behavior for different sampling frequency (Fs)

range is [1.28–1.69] kHz. Finally, for the 100 kHz, the peak frequency value is 1.470 kHz and frequency range is [1.35–1.92] kHz. Although the peak values are very close to the expected frequency, the frequency ranges tend to increase with decreasing sampling frequency with ranges of 0.34 kHz, 0.41 kHz and 0.57 kHz, respectively. In the case where even lower sampling frequencies are used then the multiresolution level will be lower than 120, which may affect the accuracy of the fault location.

4.7 Influence of the type of fault

The proposal of the IEC and CIGRE is that the frequency ranges of events in electrical networks are characterized as ferroresonance (0.1 Hz–1 kHz), fault clearing (50 Hz–3 kHz), line switching (50 Hz–20 kHz) and lightning surges (10 kHz–3 MHz) [36]. However, for this study, traveling waves caused by short-circuits are analyzed. This implies that other possible traveling wave generating phenomena such as lightning can be differentiated by the waveform distortion and periodicity of a TW. In addition, it has been verified that these phenomena present different spectral energies [37].

On the other hand, the simulations developed are two-phase faults (AB), since for the purposes of this study only the characteristics of aerial modal components are analyzed. This can be replicated in the ground modal component and thus identify the type of fault (three-phase, two-phase, two-phase to ground or single-phase to ground). For this development, the modal loops must be analyzed. However, this is not part of the scope of this paper because the aim here is to characterize the fault location.

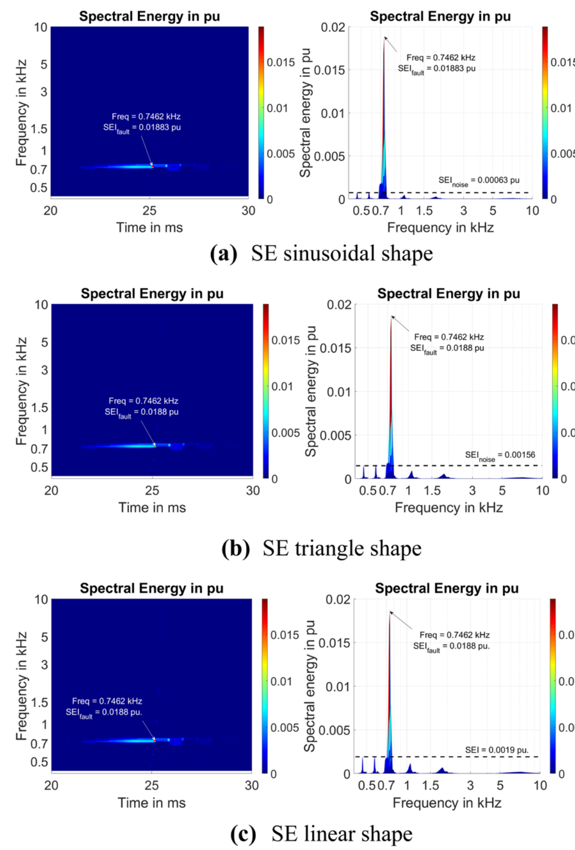

Fig. 18 Spectral energy behavior for different SE shapes

4.8 Influence of the SE shape

The SE shape is a parameter to be considered, since this function correlates with the main function. Based on the theoretical principles of the MM, the use of SE shapes similar to the main signal is proposed. However, the transient behavior caused by traveling waves presents a distorted characteristic where the impact of a TW causes a steep fall or rise in the signal and this changes each time more TWs arrive. Therefore, as the main signal is treated as a one-dimensional function, three geometric shapes described in (11)–(13) are considered. These events are developed for a fault located at 99 km.

From Fig. 18, it can be concluded that the variation for each case is not very high, as in all three cases the traveling wave frequency can be identified. However, the case of the linear function presents slightly more noise than the others.

4.9 Influence of a line with series compensation and parallel lines coupling effect

This analysis is performed on a 220 kV electrical system as shown in Fig. 19. The lines (Line 1 and 2) are 300 km long and the series capacitor represents 65% of the total line impedance. The TW speed and the line characteristic impedance are determined by inductance (L) and capacitance (C). Then the following values are obtained for both modes: $L_1 = 1.03$ mH/km and $C_1 = 0.011$ uF/km, and thus $v_1 = 292{,}379$ km/s and $Z_1 = 301.16\ \Omega$; $L_0 = 3.63$ mH/km and $C_0 = 0.006$ uF/km, and thus $v_0 = 214{,}124$ km/s and $Z_0 = 777\ \Omega$.

Based on the calculated values, the frequency vs. fault location curve is determined and is shown in Fig. 20. In addition, two fault points are considered for analysis (50 km and 150 km) and the theoretical TW frequency is determined for the aerial mode. The ground mode has a lower speed and depends on the resistivity of the ground, and therefore the curve will only be based on the aerial mode.

A two-phase fault (AB) is simulated at 150 km and 50 km from Bus R on Line 1. The voltage and current signals are shown in Fig. 21. It can be seen that the voltage behavior does not decrease as expected because of the capacitive effect. However, the transient behavior is present.

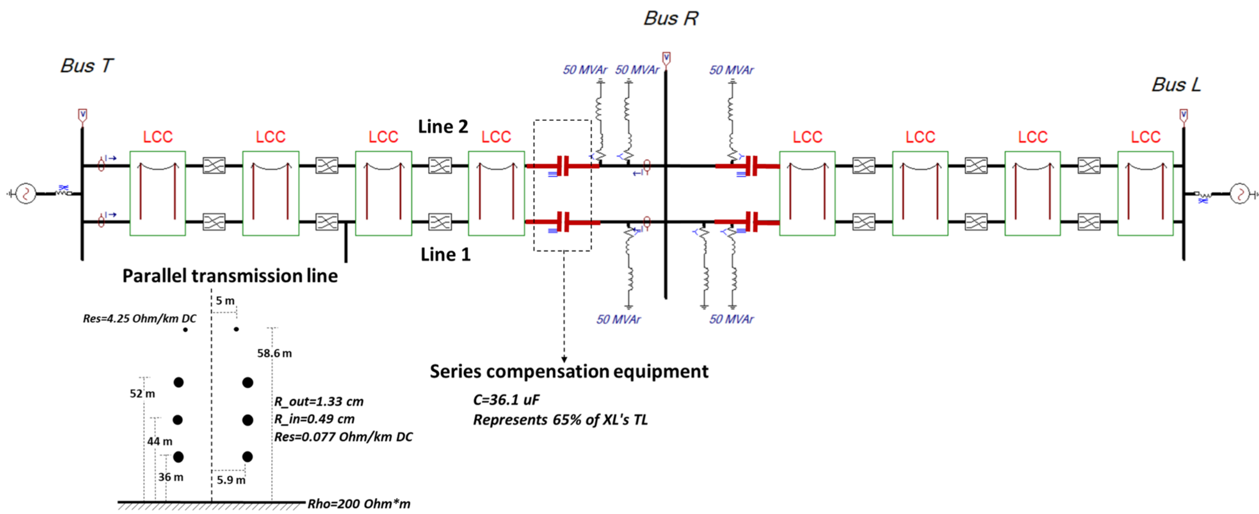

Fig. 19 Electrical system with parallel transmission lines and series compensation

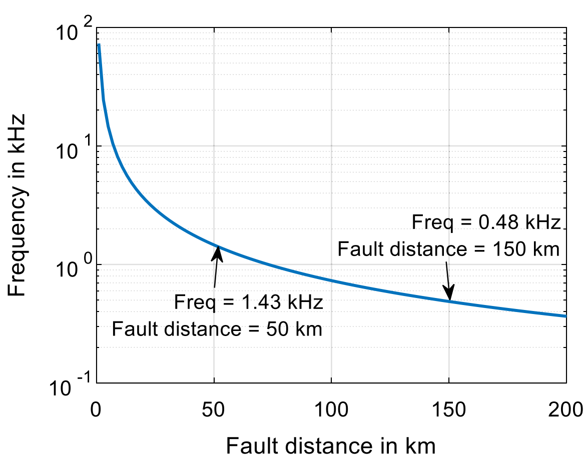

Fig. 20 TW frequency behavior for different fault distance

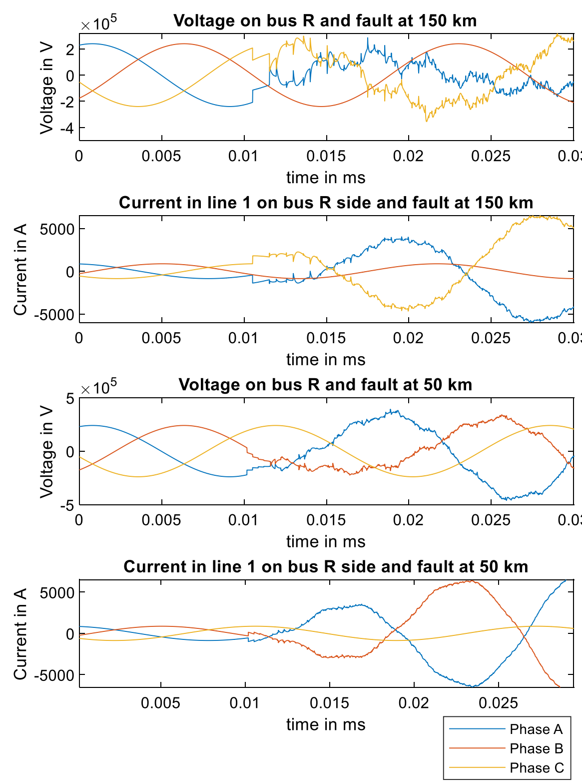

Fig. 21 Transient behavior of voltage and current signals for faults at 150 km and 50 km

For the 150 km fault, the results show that the TW frequency has a value of 0.47 kHz (see Fig. 22). This value is very close to the theoretical value (0.48 kHz) which implies that the error rate is 2%.

For the 50 km fault, the results show that the TW frequency has a value of 1.5 kHz (see Fig. 23), which is very close to the theoretical value (1.43 kHz) implying an error rate of 4.6%.

Series compensation consists of series capacitors, metal oxide varistors (MOV) and a spark gap. In the fundamental frequency domain, the effect of the series capacitor can be included, while in the high-frequency domain, the behavior of the capacitors has low capacitive impedance, and this can be considered a short-circuit. Therefore, the series capacitor does not affect the high-frequency analysis. The MOV is highly nonlinear and serves as a capacitor bank bridge during the occurrence of a fault and the spark gap is used for MOV protection. The delay time to start the MOV conduction and then the delay time to close the spark gap should

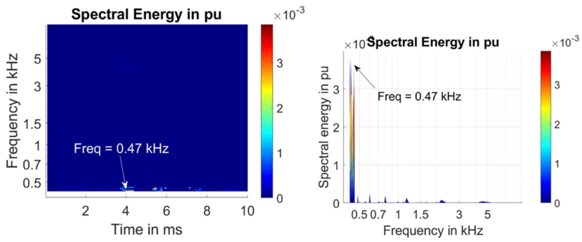

Fig. 22 Spectral energy behavior for fault at 150 km

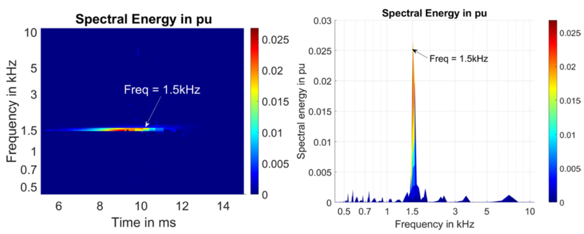

Fig. 23 Spectral energy behavior for fault at 50 km

be taken into account as the maximum time window for the analysis on lines with series compensation.

In three-phase transmission lines, the traveling waves are mutually coupled, and therefore the speed is susceptible to change. To apply the traveling wave method in three-phase systems with mutual coupling including parallel lines, the generated high-frequency signal is decomposed into its modal components (ground and aerial mode) by means of modal transformation matrices or Clarke's transformation. This effect does not have a great effect in the air mode, though the ground mode analysis is involved in the behavior of the resistivity value and this can imply changes in the TW speed.

5 Conclusion

This work develops a time–frequency analysis of high-frequency signals caused by short-circuits in transmission lines in order to characterize the fault location. For this purpose, a digital filter based on the theory of mathematical morphology and spectral energy indices is developed and thereby the multiresolution signals are determined. The results show adequate performance while allowing identification of the fault location with percentages lower than 2.68% for the high-resolution zone and with 120 multi-resolution levels. Therefore, it is useful for identifying internal and external faults. Tests for different conditions such as different resistances, inception angles, noises, sampling frequencies, and SE shapes verify that in all cases it is possible to characterize the traveling wave frequency of the signal and consequently the fault location. This method can be adapted as a fault locator for off-line analysis by increasing the multiresolution levels (> 120) and the time window up to 10 ms, as well as a protection relay by decreasing the number of multiresolution levels (< 120) and increasing the resolution at the border of the line while keeping the 5 ms time window. This will be useful for identifying internal and external faults both from one side of the line.

Through technological advances and the updating of equipment, e.g., the new optical voltage and current measuring transformers, which are emerging in the market, it is possible to obtain data from high-frequency signals, especially traveling waves, with high precision. This makes feasible the inclusion of such new algorithms that take advantage of these technologies.

Acknowledgements
Institute of electrical power systems and high voltage engineering, TU Dresden.

Author contributions
All authors read and approved the final manuscript.

Funding
German academic exchange service (DAAD) and CONICET.

Availability of data and materials
Not applicable.

Declaration

Competing interests
The authors declare that they have no known competing financial interests or personal relationships that could have appeared to influence the work reported in this paper.

Received: 22 November 2022 Accepted: 27 April 2023
Published online: 19 May 2023

References

1. Martins, J. F., Romero-Cadaval, E., Vinnikov, D., & Malinowski, M. (2022). Transactive energy: Power electronics challenges. *IEEE Power Electronics Magazine, 9*(1), 20–32. https://doi.org/10.1109/MPEL.2022.3140981
2. Quispe, J. C., & Orduña, E. (2022). Transmission line protection challenges influenced by inverter-based resources: A review. *Protection and Control of Modern Power Systems, 7*(1), 1–17. https://doi.org/10.1186/S41601-022-00249-8
3. Tse, C. K., Huang, M., Zhang, X., Liu, D., & Li, X. L. (2020). Circuits and systems issues in power electronics penetrated power grid. *IEEE Open Journal of Circuits and Systems, 1*, 140–156. https://doi.org/10.1109/OJCAS.2020.3020633
4. Vargas, W. E., & Juan Quispe, H. C. (2018). Economic benefit and improve of stability in the power system through the ultra-high speed fault clearing in transmission lines. https://doi.org/10.1109/INTERCON.2018.8526425.
5. Swift, G. W. (1979). The spectra of fault-induced transients. *IEEE Transactions on Power Apparatus and systems, 3*, 940–947. https://doi.org/10.1109/TPAS.1979.319251
6. Girgis, A. A., & Brown, R. G. (1983). Modelling of fault-induced noise signals for computer relaying applications. *IEEE Transactions on Power Apparatus and Systems, 9*, 2834–2841. https://doi.org/10.1109/TPAS.1983.318170
7. Pinto de Sa, J. L. (1992). The stochastic modeling of fault-induced transients. *IEEE Transactions on Power Delivery, 7*(3), 1156–1166. https://doi.org/10.1109/61.141826

8. Wang, X. G., Huang, S. F., & Liu, Q. K. (2008). Study of transient spectrum in transmission lines. In *IEEE Power Energy Soc. 2008 Gen. Meet. Convers. Deliv. Electr. Energy 21st Century, PES*. https://doi.org/10.1109/PES.2008.4595997.
9. He, S. Y., Cozza, A., & Xie, Y. Z. (2020). On the spatial resolution of fault-location techniques based on full-fault transients. *IEEE Transactions on Power Delivery, 35*(3), 1527–1540. https://doi.org/10.1109/TPWRD.2019.2949914
10. Huang, S. F., & Wang, X. G. (2009). A protection scheme for phase-to-phase faults based on spectrum characteristic of fault-generated high-frequency transient signals. In *2009 IEEE Power Energy Soc. Gen. Meet. PES '09, 2009*. https://doi.org/10.1109/PES.2009.5275917.
11. Nie, Y., Liu, Y., Lu, D., & Wang, B. (2021). An improved natural frequency based transmission line fault location method with full utilization of frequency spectrum information. *IET Generation, Transmission and Distribution, 15*(19), 2787–2803. https://doi.org/10.1049/GTD2.12215
12. Islam, M. M., Sanjeevikumar, P., Pedersen, J. K., & Brice, C. W. (2019). Advanced digital signal processing based transmission line fault detection and classification. In *IECON Proc. (Industrial Electron. Conf., vol. 2019-October* (pp. 4991–4996). https://doi.org/10.1109/IECON.2019.8927552.
13. Iurinic, L. U., Ferraz, R. G., & Bretas, A. S. (2013). Characteristic frequency of travelling waves applied for transmission lines fault location estimation. In *2013 IEEE Grenoble Conf. PowerTech, POWERTECH 2013, 2013*. https://doi.org/10.1109/PTC.2013.6652396.
14. Huang, S. F., & Wang, X. G. (2009). A fault location scheme based on spectrum characteristic of fault-generated highfrequency transient signals. In *2009 IEEE Power Energy Soc. Gen. Meet. PES '09, 2009*. https://doi.org/10.1109/PES.2009.5275918.
15. Okamura, M., Andow, F., Mitani, I., Okita, Y., & Masui, M. (1980). Development of new relays with significantly improved performance against badly distorted transient waveforms. *IEEE Transactions on Power Apparatus and Systems, 4*, 1426–1436. https://doi.org/10.1109/TPAS.1980.319565
16. Jafarian, P., & Sanaye-Pasand, M. (2013). High-frequency transients-based protection of multiterminal transmission lines using the SVM technique. *IEEE Transactions on Power Delivery, 28*(1), 188–196. https://doi.org/10.1109/TPWRD.2012.2215925
17. Mallat, S. G. (1989). A theory for multiresolution signal decomposition: The wavelet representation. *IEEE Transactions on Pattern Analysis and Machine Intelligence, 11*(7), 674–693. https://doi.org/10.1109/34.192463
18. Wang, X., Qian, Q., & Chen, W. (2002). Analyzing fault-induced transients with wavelets. In: *Proc. IEEE Power Eng. Soc. Transm. Distrib. Conf.* (Vol. 3, No. SUMMER, pp. 1090–1093). https://doi.org/10.1109/PESS.2002.1043430.
19. Hisakado, T., Tanaka, K., & Okumura, K. (2002). A transmission line fault-location system using the wavelet transform. *Electrical Engineering in Japan, 140*(4), 27–37. https://doi.org/10.1002/EEJ.10040
20. Hisakado, T., & Okumura, K. (2001). An application of wavelet transform to fault location and its implementation on FPGA. In *Midwest Symp. Circuits Syst.* (Vol. 2, pp. 528–531). https://doi.org/10.1109/MWSCAS.2001.986246.
21. Crossley, P. A., & McLaren, P. G. (1983). Distance protection based on traveling waves. *IEEE Power Engineering Review, 9*, 30–31. https://doi.org/10.1109/MPER.1983.5519286
22. Liang, R., Wang, Z., Peng, N., Zare, F., Liu, X., & Liu, C. (2018). Traveling wave protection based on asynchronously sampled time difference of arrival of modulus traveling waves in per unit line length. *Electric Power Systems Research, 165*, 250–258. https://doi.org/10.1016/J.EPSR.2018.08.013
23. Bo, Z. Q., Redfern, M. A., & Weller, G. C. (2000). Positional protection of transmission line using fault generated high frequency transient signals. *IEEE Transactions on Power Delivery, 15*(3), 888–894. https://doi.org/10.1109/61.871348
24. Islam, M., Mohammadpour, H. A., Ghaderi, A., Brice, C. W., & Shin, Y. J. (2015). Time-frequency-based instantaneous power components for transient disturbances according to IEEE standard 1459. *IEEE Transactions on Power Delivery, 30*(3), 1288–1297. https://doi.org/10.1109/TPWRD.2014.2361203
25. Zou, L., Zhao, Q., Lin, X., & Liu, P. (2005). Applications of multi-resolution morphological analysis in ultra high speed protection of transmission line. In *2005 IEEE Power Eng. Soc. Gen. Meet.* (Vol. 1, pp. 707–713). https://doi.org/10.1109/PES.2005.1489252.
26. Zhang, L. L., Li, M. S., Ji, T. Y., Wu, Q. H., Jiang, L., & Zhan, J. P. (2014). Morphology singular entropy-based phase selector using short data window for transmission lines. *IEEE Transactions on Power Delivery, 29*(5), 2162–2171. https://doi.org/10.1109/TPWRD.2014.2301231
27. Luo, X., Zhang, L., Shan, H., & Ji, T. (2022). Traveling wave velocity independent fault location scheme with adaptive mathematical filters for distribution network. *Electric Power System Research, 209*, 108040. https://doi.org/10.1016/J.EPSR.2022.108040
28. Singh, G. K., & Singh, D. (2012). Modeling and testing of multi-resolution morphological gradient distance relay algorithm. *Energy Procedia, 14*, 271–279. https://doi.org/10.1016/J.EGYPRO.2011.12.929
29. Gautam, S., & Brahma, S. M. (2009). Overview of mathematical morphology in power systems—A tutorial approach. In *2009 IEEE Power Energy Soc. Gen. Meet. PES '09, 2009*. https://doi.org/10.1109/PES.2009.5275190.
30. Matheron, G., & Serra, J. (1998). The birth of mathematical morphology, Ec. des Mines Paris, Cent. Morphol. Mathématique.
31. Ji, Z., Bai, N., Li, Q., & Wu, Q. H. (2007). A soft morphological filter for periodic noise reduction. *Chinese Journal of Electronics, 16*(2), 289–294.
32. Zhang, J., Zeng, Z., Zhang, L., Lu, Q., & Wang, K. (2019). Application of mathematical morphological filtering to improve the resolution of Chang'E-3 lunar penetrating radar data. *Remote Sensing, 11*, 524. https://doi.org/10.3390/RS11050524
33. Jing-Tian, T., et al. (2012). Mathematical morphology filtering and noise suppression of magnetotelluric sounding data. *Chinese Journal of Geophysics, 55*(5), 1784–1793. https://doi.org/10.6038/J.ISSN.0001-5733.2012.05.036
34. Vaidyanathan, P. P. (2001). Generalizations of the sampling theorem: Seven decades after Nyquist. *IEEE Transactions on Circuits and Systems I: Fundamental Theory and Applications, 48*(9), 1094–1109. https://doi.org/10.1109/81.948437
35. Quispe, J. C. H., Morales, J., & Orduna, E. (2022). MRA of Fault-generated High-frequency transient signals using mathematical morphology. comparison with wavelet transform (pp. 1–8). https://doi.org/10.1109/ARGENCON55245.2022.9939830.
36. Martinez, J. A., Mahseredjian, J., & Walling, R. A. (2005). Parameter determination: Procedures for modeling system transients. *IEEE Power Energy Magazine, 3*(5), 16–28. https://doi.org/10.1109/MPAE.2005.1507018
37. Liang, Z., Zhu, Y., Dai, L., Wen, Q. (2013). Identification of lightning strikes on transmission lines based on mathematical morphology and integral method. In *IET Conf. Publ.* (Vol. 2013, No. 623 CP). https://doi.org/10.1049/CP.2013.1727.